

# Low-frequency study of two Giant Radio Galaxies: 3C35 and 3C223

E. Orrù<sup>1,2</sup>, M. Murgia<sup>3,4</sup>, L. Feretti<sup>4</sup>, F. Govoni<sup>3</sup>, G. Giovannini<sup>4,5</sup>, W. Lane<sup>6</sup>, N. Kassim<sup>6</sup>, and R. Paladino<sup>1</sup>

<sup>1</sup> Institute of Astro- and Particle Physics, University of Innsbruck, Technikerstrasse 25/8, A-6020, Innsbruck, Austria

<sup>2</sup> Radboud University Nijmegen, Heijendaalseweg 135, 6525 AJ Nijmegen, The Netherlands

<sup>3</sup> INAF - Osservatorio Astronomico di Cagliari, Loc. Poggio dei Pini, Strada 54, I-09012 Capoterra (CA), Italy

<sup>4</sup> INAF - Istituto di Radioastronomia, Via Gobetti 101, I-40129 Bologna, Italy

<sup>5</sup> Dipartimento di Astronomia Università degli Studi di Bologna, Via Ranzani 1, 40127 Bologna, Italy

<sup>6</sup> Naval Research Laboratory, Code 7213, Washington DC 20375-5320, USA

Received; accepted

## ABSTRACT

**Aims.** Radio galaxies with a projected linear size  $\geq 1$  Mpc are classified as giant radio sources. According to the current interpretation these are old sources which have evolved in a low-density ambient medium. Since radiative losses are negligible at low frequency, extending spectral ageing studies in this frequency range will allow to determine the zero-age electron spectrum injected and then to improve the estimate of the synchrotron age of the source.

**Methods.** We present Very Large Array images at 74 MHz and 327 MHz of two giant radio sources: 3C35 and 3C223. We performed a spectral study using 74, 327, 608 and 1400 GHz images. The spectral shape is estimated in different positions along the source.

**Results.** The radio spectrum follows a power-law in the hot-spots, while in the inner region of the lobe the shape of the spectrum shows a curvature at high frequencies. This steepening is in agreement with synchrotron aging of the emitting relativistic electrons. In order to estimate the synchrotron age of the sources, the spectra have been fitted with a synchrotron model of emission. Using the models, we find that 3C35 is an old source of  $143 \pm 20$  Myr, while 3C223 is a younger source of  $72 \pm 4$  Myr.

**Key words.** Instrumentation: interferometers - Techniques: interferometric - Astroparticle physics - Galaxies: active - Radio continuum: galaxies - Radiation mechanisms: non - thermal

## 1. Introduction

According to the standard model of active galactic nuclei (AGNs), at the center of active galaxies resides a super-massive black hole. The AGN is powered by an accretion disk surrounded by a torus of gas and dust (Blandford & Rees 1974). The powerful radio emission observed in classical double radio sources is produced by a bipolar pair of jets; relativistic outflows of matter which originate in the AGN. They first propagate in the interstellar medium (ISM) and then in the intergalactic medium (IGM) for a typical time of  $10^8$  yr (Scheuer 1974). The hot-spots are the regions where the energy carried by the jets is diffused into the radio lobes. The observed diffuse radio emission is produced in the 'cocoon' or lobe, which is formed by the built up jet material and/or energy in the region between the core and the hot-spots. The energy evolution of the cocoon can be traced by observations and spectral studies of the radio lobes. Radio lobes expand, and, assuming the source is in the equipartition regime, the pressure of the relativistic plasma in the lobe equals the pressure of the external environment (Begelman et al. 1984).

The radio spectrum of radio galaxies is initially described by a power-law. The final shape of the spectrum moves away from the power-law showing a steepening at higher frequencies. This is due to the competition between processes of energy injection and losses due to adiabatic expansion, synchrotron emission and inverse Compton scattering with the CMB photons, (Kardashev 1962; Kellermann 1964; Pacholczyk 1970). The initial models developed to interpret these spectra assumed a uniform and con-

stant magnetic field and an isotropic injection of electrons (e.g., Kardashev 1962; Pacholczyk 1970; Jaffe & Perola 1973, hereafter KP and JP). If the former assumptions are satisfied it is possible, in theory, to use the synchrotron spectrum to estimate the age of the radiating particles.

Many authors (e.g., Tribble 1993; Eilek et al. 1997; Blundell & Rawlings 2000) argue that the observed filamentary structures in the radio lobes (e.g. for Cygnus A, Carilli et al. 1991) can be interpreted as the effect of inhomogeneous magnetic fields on the synchrotron emission. However, Kaiser (2000) demonstrated that the spatial distribution of the synchrotron radio emission can be used to estimate the age for FR II sources (Fanaroff & Riley 1974). Furthermore, based on the dynamical and radiative self-similar models in Kaiser & Alexander (1997) and Kaiser et al. (1997), Kaiser (2000) developed a 3-dimensional model of the synchrotron emissivity of the cocoons of powerful FR II radio sources. The projection along the line of sight (LOS) of the 3D model can be easily compared with radio observations.

X-ray emission related to the lobes has been detected in a number of radio sources. This is attributed to the inverse Compton (IC) scattering of microwave background photons. The direct estimates of the magnetic field ( $B_{IC}$ ) obtained from the combination of the X-ray IC flux and the radio synchrotron spectrum, give values near to those found with the equipartition ( $B_{eq}$ ) assumption (e.g., Croston et al. 2004, 2005). Moreover, the above-mentioned comparisons suggest that lobes are not overpressured at the late stages of evolution of radio galaxies (Croston et al. 2004, 2005; Konar et al. 2009). On the other hand, a strong variation of the X-ray/radio flux ratio across the lobes

Send offprint requests to: E. Orrù e.orrù@astro.ru.nl

**Table 1.** Summary of radio observations and images. Col. 1: source name; Col. 2, 3: radio pointing position; Col. 4: observing frequency; Col. 5: bandwidth; Col. 6: date of observations; Col. 7: time of integration; Col. 8: VLA configuration; Col. 9: resolution; Col. 10: Position Angle; Col. 11:rms.

Name	$\alpha$ (J2000) (h m s)	$\delta$ (J2000) (° ' ")	$\nu$ MHz	$\Delta\nu$ MHz	Date	Duration hours	Array	HPBW "×"	PA °	rms mJy/beam
3C35	01 12 02.20	+49 28 35.00	73.8	1.562	23-11-2003	6	B	93×64	-85	95
			327.5	3.125	23-11-2003	6	B	23×17	-85	1.3
			327.5-321.5	3.125	21-03-2004	3.5	C	55×50	15	2.3
			327.4	3.125		9.5	B+C	27×21	-88	1.0
3C223	09 39 52.74	+35 53 58.20	73.8	1.562	16-11-2004	5	A	25×24	-58	43
			73.8	1.562	03-03-2005	5	B	83×73	-62	98
			73.8	1.562		10	A+B	26×25	-61	40
			327.3	6.25	16-12-2004	5	A	6×5	-77	0.7
			328.9	6.25	03-03-2005	5	B	19×16	-82	1.3
			327.3	6.25		10	A+B	7×6	-78	0.6

**Table 2.** Sources properties.

Name	$\alpha$ (J2000) (h m s)	$\delta$ (J2000) (° ' ")	$z$	kpc/'	LAS '	LLS kpc	$L_{178\text{ MHz}}$ $\text{W Hz}^{-1}$
3C35	01 12 02.23	+49 28 35.2	0.0673	1.273	12.5	950	$10^{26.09}$
3C223	09 39 52.74	+35 53 58.2	0.1368	2.393	5.4	780	$10^{26.89}$

Col. 1: source name; Col. 2: and 3: source coordinates from NASA/IPAC extragalactic database (NED) ; Col. 4: redshift by Burbidge & Strittmatter (1972) and Abazajian et al. (2009); Col. 5: arcsec to kpc conversion; Col. 6: largest angular size; Col. 7: largest linear size; Col. 8: radio luminosity at 178 MHz (Laing & Peacock 1980).

has been found (Isobe et al. 2002; Hardcastle & Croston 2005; Goodger et al. 2008). This cannot be explained with models in which either the electron energy spectrum or the magnetic field vary independently as function of position in the lobes, but it is consistent with models in which both vary together as function of position.

Among radio galaxies (RG), those with a projected linear size  $\geq 1 \text{ Mpc}^1$  are defined as giant radio galaxies (GRG). In the complete sample of 3CR radio sources (Laing et al. 1983) around 6% of the sources are giants; there are about 100 known. GRG typically have radio powers below  $10^{26.5} \text{ W Hz}^{-1} \text{ sr}^{-1}$ , have linear sizes less than 3 Mpc, and are observed at redshifts  $z < 0.25$ , even though  $z < 0.5$  could be assumed as an upper limit (Ishwara-Chandra & Saikia 1999; Schoenmakers et al. 2000; Lara et al. 2004; Saripalli et al. 2005; Machalski et al. 2007). The P-D diagram (Lara et al. 2004; Ishwara-Chandra & Saikia 1999) shows a dearth of high luminosity GRG, as predicted by evolutionary models (Blundell et al. 1999; Kaiser et al. 1997) and a maximum GRG linear size cut off of 3 Mpc. An estimate of the predominant process of radiative losses, obtained by separating the contributions of the inverse Compton and synchrotron losses, shows that the ratio of the estimated  $B_{\text{CMB}}/B_{\text{eq}}$  increases with linear size, and IC losses dominate the radiative losses in GRG (Ishwara-Chandra & Saikia 1999).

As argued by many authors, the observed physical characteristics mentioned above could be the result of selection effects introduced by the selection criteria or by biases due to the low sensitivity of typical radio images. The faintest regions of GRG are

well detected, even with a modest angular resolution, only with low frequency interferometric observations. The low-frequency spectral index information is crucial to derive the energy distribution of the radiating electrons, and to study the energy transport from the nucleus to the lobes in these exceptionally large radio sources. Multifrequency spectral aging studies of GRG have been recently presented by Jamrozny and collaborators (Jamrozny et al. 2004, 2005, 2008). The median value for the estimated spectral ages is 23-24 Myr. The injection spectral index ranges from 0.55 to 0.88; it appears to increase with luminosity and redshift but shows an inverse correlation with linear size.

In this paper we present a multifrequency spectral analysis of two classical double giant radio galaxies 3C35 and 3C223. In Sect. 2 radio observations and data analysis at 74 and 327 MHz are described. In Sect. 3 we present radio images of 3C35 and 3C223 at 74 and 327 MHz. In Sect. 4 we show the spectral index maps and the spectral analysis obtained by combining images at 74, 327, 608 and 1400 MHz. Results are discussed and summarized in Sect. 5.

## 2. Radio Data

The two selected giant radio galaxies are 3C35 and 3C223. 3C35 is included in the sample of 47 low redshift ( $z < 0.4$ ) GRG obtained by Schoenmakers et al. (2001) using the Westerbork Northern Sky Survey (WENSS) of the sky above  $+30^\circ$  of declination at 325 MHz (Rengelink et al. 1997). The criteria for the sample specified that a candidate GRG must have: *i*) an angular size larger than 5 arcminutes, and *ii*) a distance to the galactic plane of more than 12.5 degree.

3C223 is included in a complete sample of large scale radio sources selected by Leahy & Perley (1991). The sources are

<sup>1</sup> Throughout we adopt  $H_0 = 71 \text{ km s}^{-1} \text{ Mpc}^{-1}$ ,  $\Omega_m = 0.27$ ,  $\Omega_\Lambda = 0.73$  (Spergel et al. 2003). Many radio galaxies have been classified as giant in the past using a different set of cosmological parameters. For this reason some GRG could have a linear size slightly less than 1Mpc.

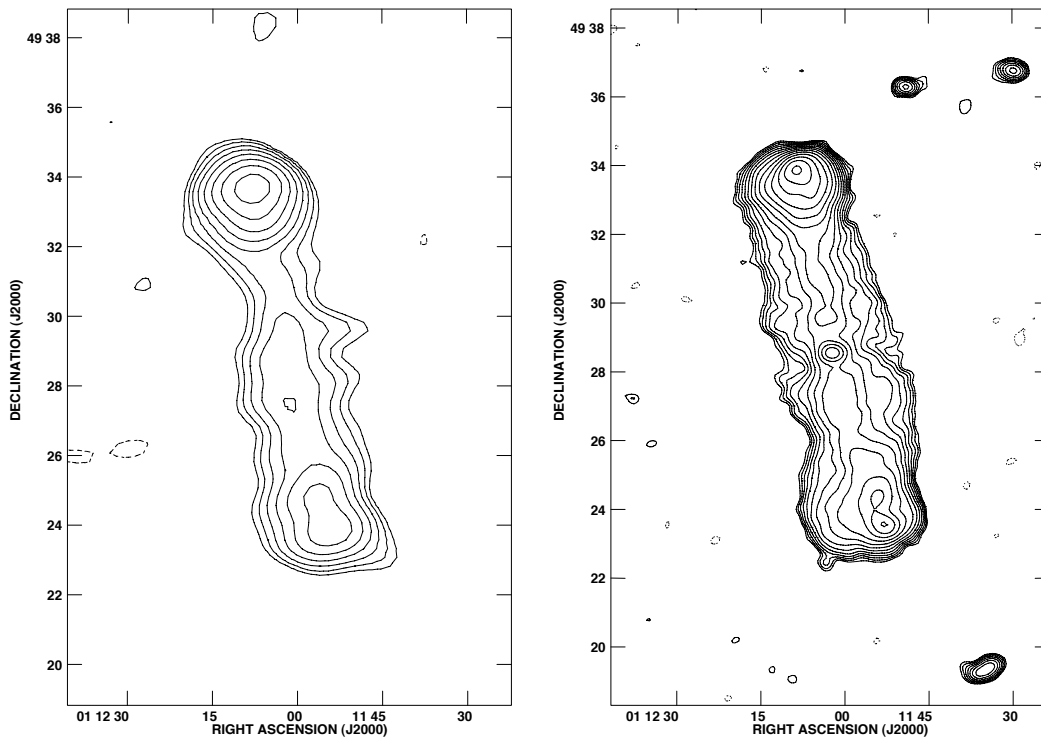


**Fig. 1.** Radio images of 3C35, all contours start at  $(3\sigma)$  and are scaled by  $\sqrt{2}$ . *Left:* VLA image at 74 MHz; the resolution is  $93'' \times 64''$  with a  $PA = -85^\circ$ , and the first two levels are at  $-285$  and  $285$  mJy/beam. *Right:* 327 MHz VLA image. The image is obtained by combining the B and C configuration data, and the resolution is  $27'' \times 21''$  with a  $PA = -88^\circ$ . The first two levels of contours are  $-3$  and  $3$  mJy/beam.

drawn from a subset of the complete radio sample with  $z$  less than 0.5 defined by Laing et al. (1983).

3C35 and 3C223 have linear sizes of 950 kpc and 780 kpc respectively, with the adopted cosmological parameters.

We observed these two GRG with the Very Large Array at 74 and 327 MHz in several configurations, according to their angular dimensions, in order to avoid the loss of flux. Observational parameters are summarized in Table 1. Since observations were made at slightly different frequencies, we will refer in the text simply to observations at 74 and 327 MHz. The exact frequencies are reported in section 3 and are used for estimates of the physical parameters.

### 2.1. Observing strategy

Radio Frequency Interference (RFI) strongly affects and corrupts the data in low-frequencies observations. In order to permit the RFI excision and to minimize the bandwidth smearing effect, the observations were conducted in spectral line mode. A difference has been established in the nature of the RFI sources in the VLA system: at 74 MHz most of interference is caused by the 100 kHz oscillators in the bases of each telescope, which generate harmonics at 100 kHz intervals and produce the typical “100 kHz comb”. This kind of RFI is “easy” to predict and eliminate. In the 327 MHz band, the internal electronics of the VLA gives rise to harmonics that are multiples of 5 and 12.5 MHz; to avoid these narrow bandwidths are used (Kassim et al. 1993). On the whole, the values of rms sensitivity attained at these frequencies are somewhat higher than the expected thermal noise levels, because of the contribution of several factors: confusion, broad-band RFI, and VLA generated RFI.

### 2.2. Data Reduction

Data were calibrated and reduced with Astronomical Image Processing System (AIPS). Since the calibration procedures are different for 74 MHz and 327 MHz, the following sections describe the methods employed separately.

#### 2.2.1. 74 MHz

The 74 MHz data were calibrated and imaged following the same procedure used for the VLA Low-frequency Sky Survey (VLSS) as described carefully in Kassim et al. (2007) and Cohen et al. (2007).

Both for 3C35 and 3C223 we made the amplitude and bandpass calibration using a model of Cygnus A<sup>2</sup>.

Careful data editing was used to excise the RFI (Lane et al. 2005); the percentage of flagged data at the end of this process was about 13% for both sources. Before the final imaging data were averaged to 8 frequency channels with a resolution of 170.9 kHz.

To produce the final images we used the so called “field-based calibration” method developed for the VLSS (Cotton et al. 2004). The field-based calibration procedure makes a correction for the low-order in the ionospheric terms and performs a “wide-field imaging” (kindly provided by W. D. Cotton). The offsets of the apparent positions of the NRAO VLA Sky Survey (NVSS) sources (Condon et al. 1998) from their expected positions were computed at time intervals of 2 minutes and corrected in the visibility data. Some data with too large correction were removed

<sup>2</sup> Available from <http://lwa.nrl.navy.mil/tutorial/VLAmodels>

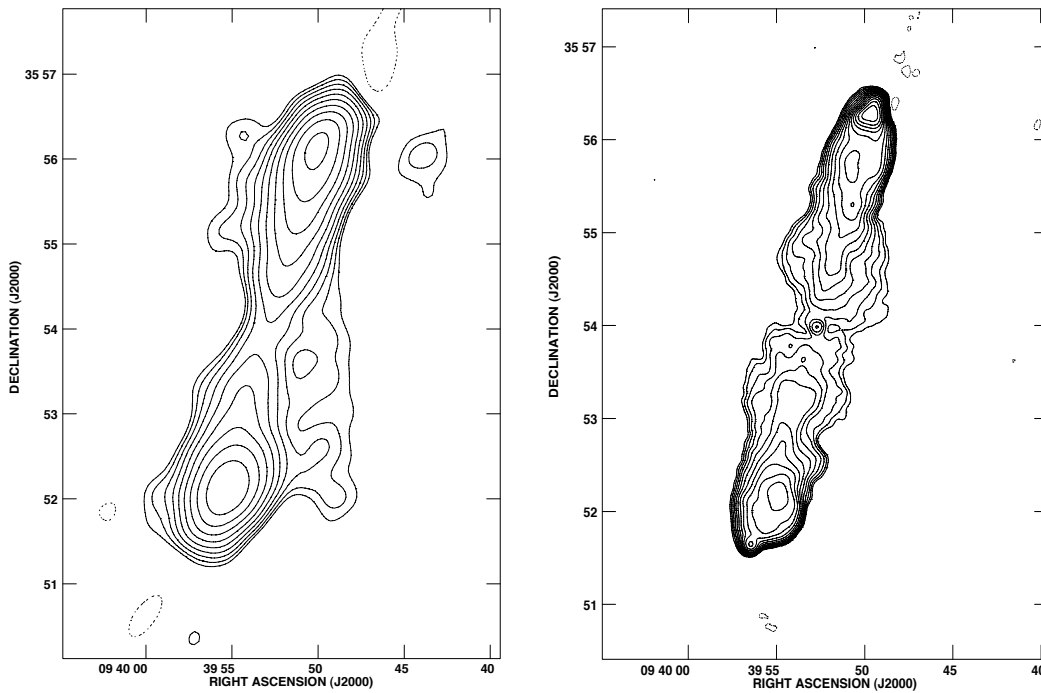


**Fig. 2.** Radio images of 3C223, all contours start at ( $3\sigma$ ) and are scaled by  $\sqrt{2}$ . *Left:* VLA image at 74 MHz. The image is obtained by combining the data of A and B configurations; the resolution is  $26'' \times 25''$  with a PA= $-61^\circ$ . The first two levels of contours are  $-120$  and  $120$  mJy/beam. *Right:* 327 MHz VLA image, obtained by combining the data of A and B configurations; the resolution is  $7'' \times 6''$  with a PA= $-78^\circ$ . The first two levels of contours are  $-1.8$  and  $1.8$  mJy/beam.

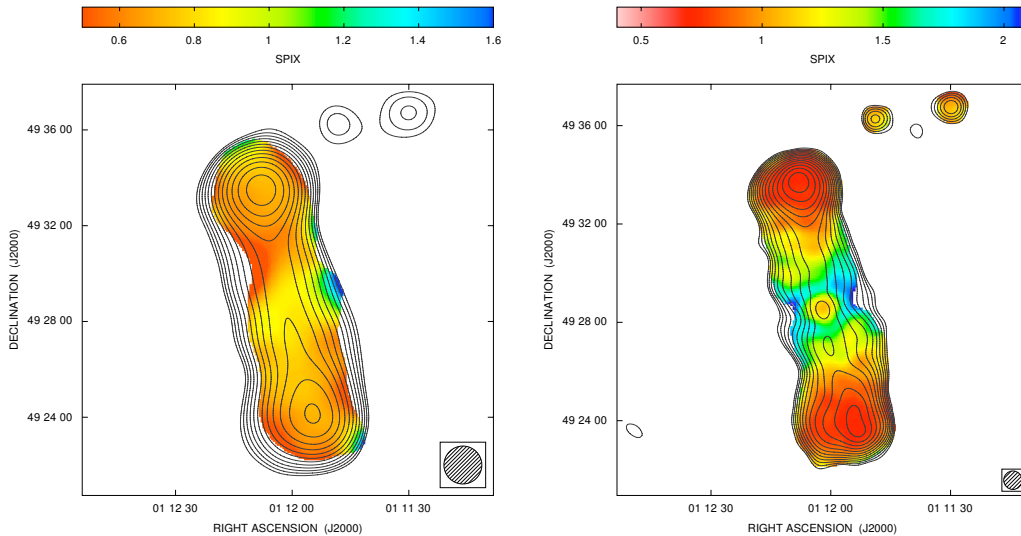


**Fig. 3.** 3C35: Spectral index maps are shown in color; pixels whose brightness was below  $3\sigma$  have been blanked. Contour levels are the radio brightness at 327 MHz, start at ( $3\sigma$ ) and are scaled by  $\sqrt{2}$ . *Left* Spectral index map between 74 MHz and 327 MHz, with a resolution of  $95'' \times 95''$ . *Right* Spectral index map between 327 MHz and 1.4 GHz, with a resolution of  $45'' \times 45''$  (the image at 1.4 GHz was taken from the NVSS (Condon et al. 1998)).

for 3C35. We corrected the final images for the primary beam effect.

The final image of 3C35 obtained with VLA data in B configuration has an rms sensitivity of  $\sim 95$  mJy/beam ( $93'' \times 64''$ ).

For the source 3C223 we produced a high resolution image in A configuration, with rms sensitivity  $\sim 43$  mJy/beam ( $25'' \times 24''$ ). A low resolution image was also made with data

from the VLA in B configuration; it has an rms sensitivity  $\sim 98$  mJy/beam ( $83'' \times 73''$ ). The image obtained with the combination of A and B configurations data has a sensitivity of 40 mJy/beam ( $26'' \times 25''$ ). The sensitivity is different from the theoretical noise because of side-lobe confusion from other sources in the beam.

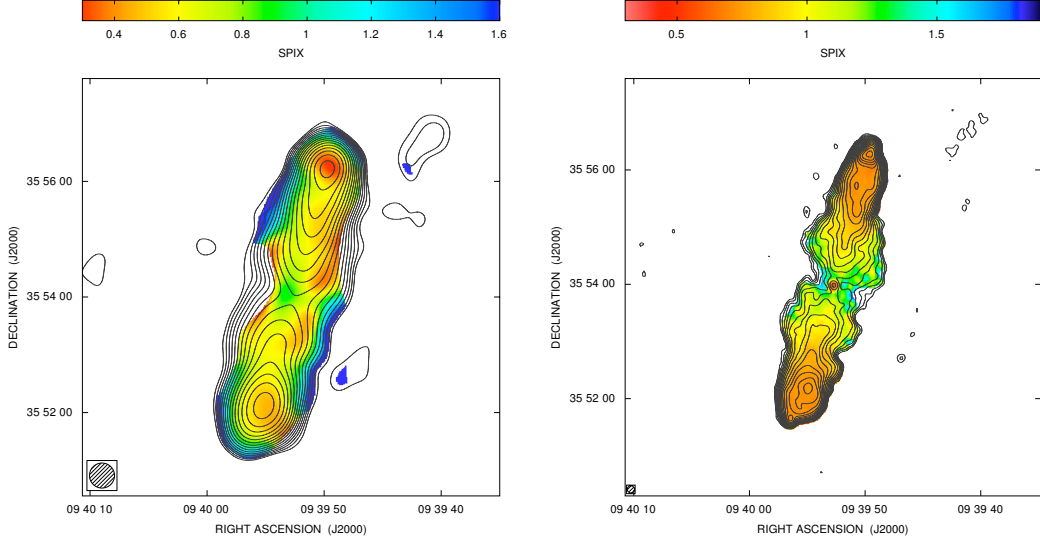


**Fig. 4.** 3C223: Spectral index maps are shown in color; pixels whose brightness was below  $3\sigma$  have been blanked. Contour levels are the radio image at 327 MHz, start at  $(3\sigma)$  and are scaled by  $\sqrt{2}$ . *Left* Spectral index map between 74 MHz and 327 MHz, with a resolution of  $26'' \times 26''$ . *Right* Spectral index map between 327 MHz and 1.48 GHz, with a resolution of  $7.5'' \times 7.5''$ .

### 2.2.2. 327 MHz

We made the amplitude and bandpass calibration with the sources 3C48 and 3C286 respectively for 3C35 and 3C223.

After careful data editing to remove RFI, 10% of data were flagged in 3C35 and 3% for 3C223.

Before imaging, the data of 3C35 were averaged to 5 channels with a resolution of 488.3 KHz, and the 3C223 data were averaged to 6 channels with a resolution of 781.3 kHz.

The data were mapped using a wide-field imaging technique, which corrects for distortions in the image caused by the non-coplanarity of the VLA over a wide field of view (the "3-D effect" included in the AIPS task IMAGR). A set of small overlapping maps was used to cover the central area of about  $\sim 1.5^\circ$  in radius (Cornwell & Perley 1992). However, at this frequency confusion lobes of sources far from the center of the field are still present. Thus, we also imaged strong sources in an area of about  $\sim 60^\circ$  in radius, based on positions in the NVSS catalog. All these "facets" were included in the CLEAN and used for several loops of self-calibration (Perley 1999). The data for each observation and configuration were calibrated, imaged and then combined. We corrected the final images for the primary beam effect.

In particular, for 3C35, we obtain a high resolution image at 327 MHz with data from the VLA in B configuration; the rms sensitivity is  $\sim 1.3$  mJy/beam ( $23'' \times 17''$ ). A low resolution image was made from VLA observations in C configuration, with an rms sensitivity of  $\sim 2.3$  mJy/beam ( $55'' \times 50''$ ). By combining the B configuration data and data from IF 1 of the C configuration, we improved the uv-coverage and sensitivity; the rms in the combined image is  $\sim 1.0$  mJy/beam ( $27'' \times 21''$ ).

We obtained a high resolution image of 3C223 with VLA observations in A configuration; the rms sensitivity is  $\sim 0.7$  mJy/beam ( $6'' \times 5''$ ). A low resolution image with a sensitivity of  $\sim 1.3$  mJy/beam was made from VLA data taken in B configuration ( $19'' \times 16''$ ). To improve the uv-coverage and the sensitivity we combined the datasets. The final rms sensitivity

is  $\sim 0.6$  mJy/beam ( $7'' \times 6''$ ). The final sensitivity differs from the theoretical noise due to classical confusion.

## 3. Results

### 3.1. 3C35

The source 3C35 is a classical double radio source with a regular FR II structure (Fanaroff & Riley 1974); its principal characteristics are listed in Table 2. It has been previously studied at frequencies of 608 MHz, 1.4 and 5 GHz with the Westerbork Synthesis Radio Telescope (WSRT) (van Breugel & Jägers 1982; Jägers 1987; Schoenmakers et al. 2000).

The VLA radio images at 74 and 327 MHz of the radio galaxy 3C35 are shown respectively in the left and in the right panel of Fig. 1; sensitivities and resolutions are listed in Table 1. On the left of Fig. 1 is the image at 73.8 MHz obtained with VLA in B configuration. In the contours map the regular double-lobe structure of the source is distinctly clear, as well as the presence of the two hot-spots. The emission is stronger at the head of the Northern lobe (N lobe).

On the right panel of Fig. 1 the 327 MHz image is shown. The image is obtained by combining the data of B and C configurations at a frequency of 327.4 MHz. The high and the low resolution images (not shown in this paper) have been obtained with the B and the C configurations of the VLA respectively. The image at 327 MHz confirms that in the N lobe the radio emission is stronger than in the Southern lobe (S lobe). The hot spot South (S hot spot) is slightly shifted with respect to the axis of symmetry of the source. Based on the images at 5 GHz, van Breugel & Jägers (1982) claimed that the S hot spot could be a double. Considering the image at 327 MHz, it seems that the second weak "hot spot" is more likely to be a knot of the jet. In the image the core and surrounding low brightness emission have both been detected.

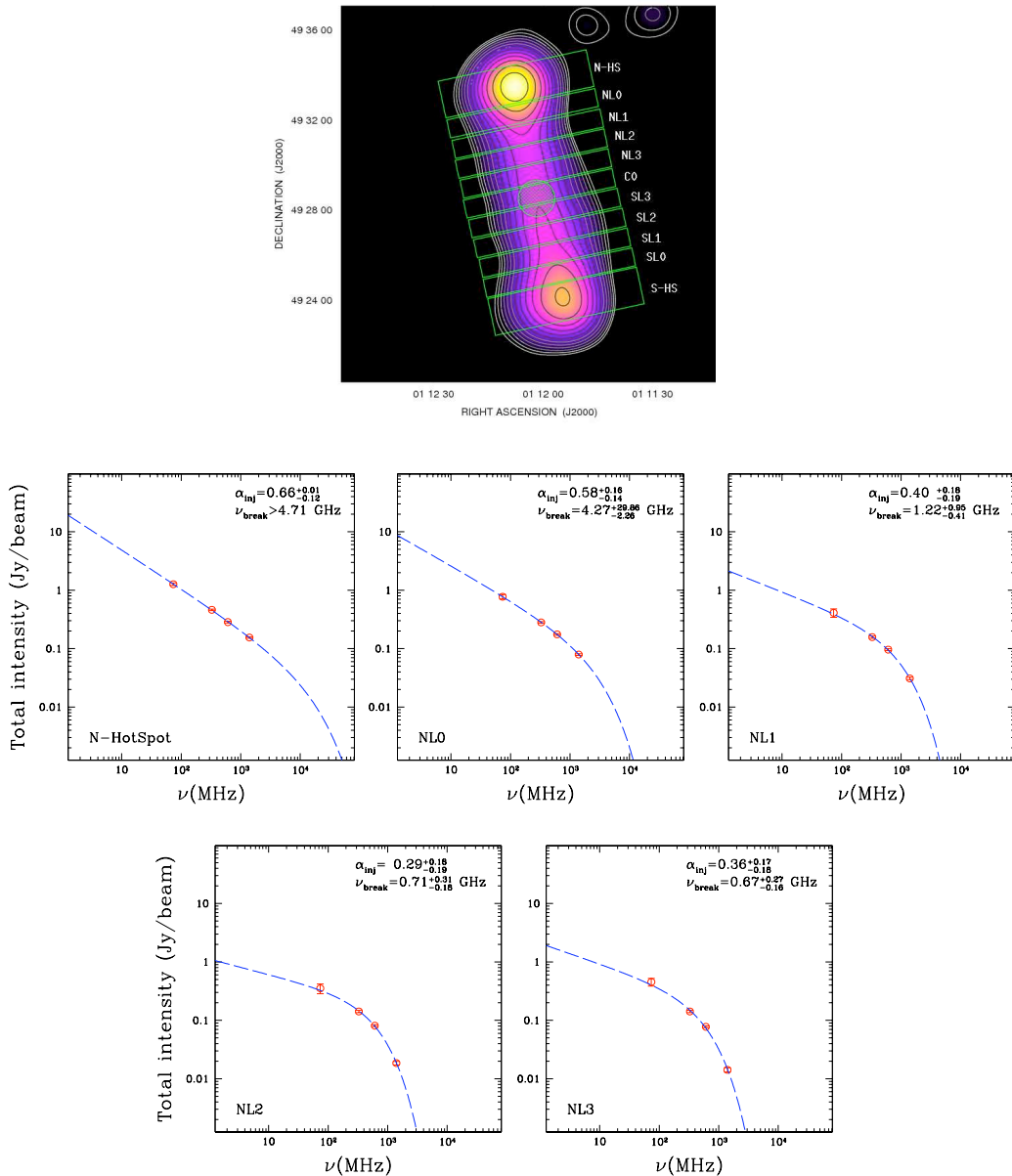


**Fig. 5. a.** 3C35: Color map of the source (resolution  $95''$ ) and the contours at 327 MHz; overlaid by the green array of boxes where the intensity measures have been taken. For the N lobe: plots represent the spectral shape of the source labeled according the positions. Points are measures taken at four frequencies, dashed lines are the fits with the synchrotron model.

### 3.2. 3C223

The host galaxy of 3C223 is in a group of 12 small galaxies (Baum et al. 1988). It is a typical double radio source with a regular FR II structure (Fanaroff & Riley 1974). It has been previously studied in with the WRST at 608 MHz, 1.4 and 5 GHz (Hogbom 1979; van Breugel & Jägers 1982; Jägers 1987) and at high resolution with the VLA at 1.4 GHz (Leahy & Perley 1991). The general characteristics of this source are presented in Table 2.

The images at 74 and 327 MHz shown in figure 2 were obtained by VLA observations using A and B configurations. The sensitivities and resolutions are listed in Table 1.

The 74 MHz image is shown on the left panel of Figure 2. A low resolution image has been obtained with the VLA in B configuration while the high resolution image has been made with

the A configuration (both images are not shown in this paper). To improve the uv-coverage and the sensitivity, we combined the A and B configuration data. The combined image, shown on the left of Fig. 2, is made at an observed frequency of 73.8 MHz.

As can be observed in the higher brightness contours of the image, the morphology of the source preserves the FR II structure. An extended low brightness structure is easily visible to the West of the southern lobe and some faint extended emission seems also to be present to the East of the northern lobe. This diffuse structure shows a different orientation axis with respect to that of the active lobes. The origin of this structure is not clear, it could be the remnant of former radio emission, or a relic lobe. A hint of this low brightness emission is present at the same position in the existing image at 1.4 GHz Leahy & Perley (1991). The estimated spectral index of this low brightnesses radio structure is  $\alpha \sim 1.3$  (obtained from the spectral index map between 1.4 GHz

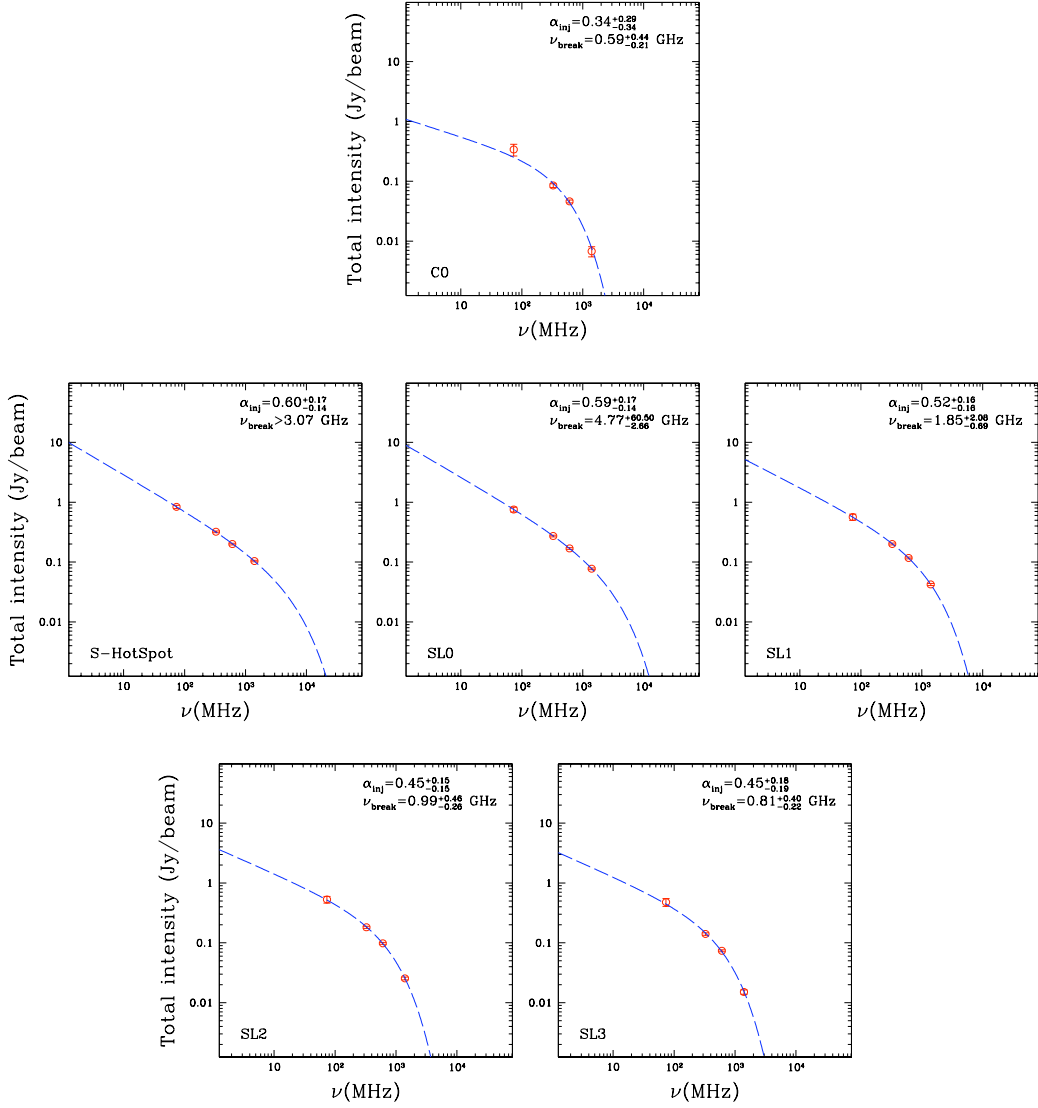


**Fig. 5. b.** Similar to Fig.5 a for the S lobe of 3C35

and 74 MHz not shown here); this is conspicuously steeper than the average value measured for the whole radio galaxy (Section 3.3 and Tab.5).

The image at 327 MHz is shown on the right panel of Figure 2. An high resolution image at 327.3 MHz has been obtained with the VLA in A configuration, while the low resolution image, obtained at the observing frequency of 328.9 MHz with the B configuration (both images are not shown in this paper). In the right panel of Figure 2 are presented the contours of the image obtained by combining the A and B configuration data at the frequency of 327.3 MHz.

Unlike the images at 608 MHz (van Breugel & Jägers 1982), the core has been clearly detected at 327 MHz thanks to the high resolution achieved. High resolution obtained in the image at 327 MHz allows to confirm the peculiar “V” shape of the N hot spot, previously seen in high-resolution images at 1.4 GHz (Leahy & Perley 1991). Moreover, at 327 MHz, as well as in the high resolution images at 1.4 and 5 GHz (van Breugel & Jägers 1982; Leahy & Perley 1991), the S hot spot seems embedded in the lobe, at the end of which a protuberance is detected.

### 3.3. Spectral index distribution

By combining the new images at 74 MHz and 327 MHz with those at 1.4 GHz available in the literature, we obtained the spectral index<sup>3</sup> distributions of the two radio galaxies 3C35 and 3C223. Figures 3 and 4 show the spectral index maps of 3C35 and 3C223, respectively. Both figures show on the left the spectral index maps between 74 MHz and 327 MHz, while on the right are those between 327 MHz and 1.4 GHz. In the range between 74 MHz and 327 MHz (95''×95''), the spectral index values of 3C35 vary from  $\alpha \sim 0.65 \pm 0.04$ , in the main parts of the source, up to  $\alpha \sim 0.84 \pm 0.06$  in the region near the core.

The spectral index between 327 MHz and 1.4 GHz (45''×45'') for 3C35 varies more than the lower frequency index. In the region of the head of the lobes,  $\alpha$  is about  $0.72 \pm 0.01$ , while it reaches values of  $\sim 1.6 \pm 0.04$  in the inner region of the lobes around the core. The image at 1.4 GHz used to obtain the spectral index map has been taken from the NVSS (Condon et al. 1998). The morphology of this source at 1.4 GHz recalls the one observed at 327 MHz.

<sup>3</sup>  $S(\nu) \propto \nu^{-\alpha}$

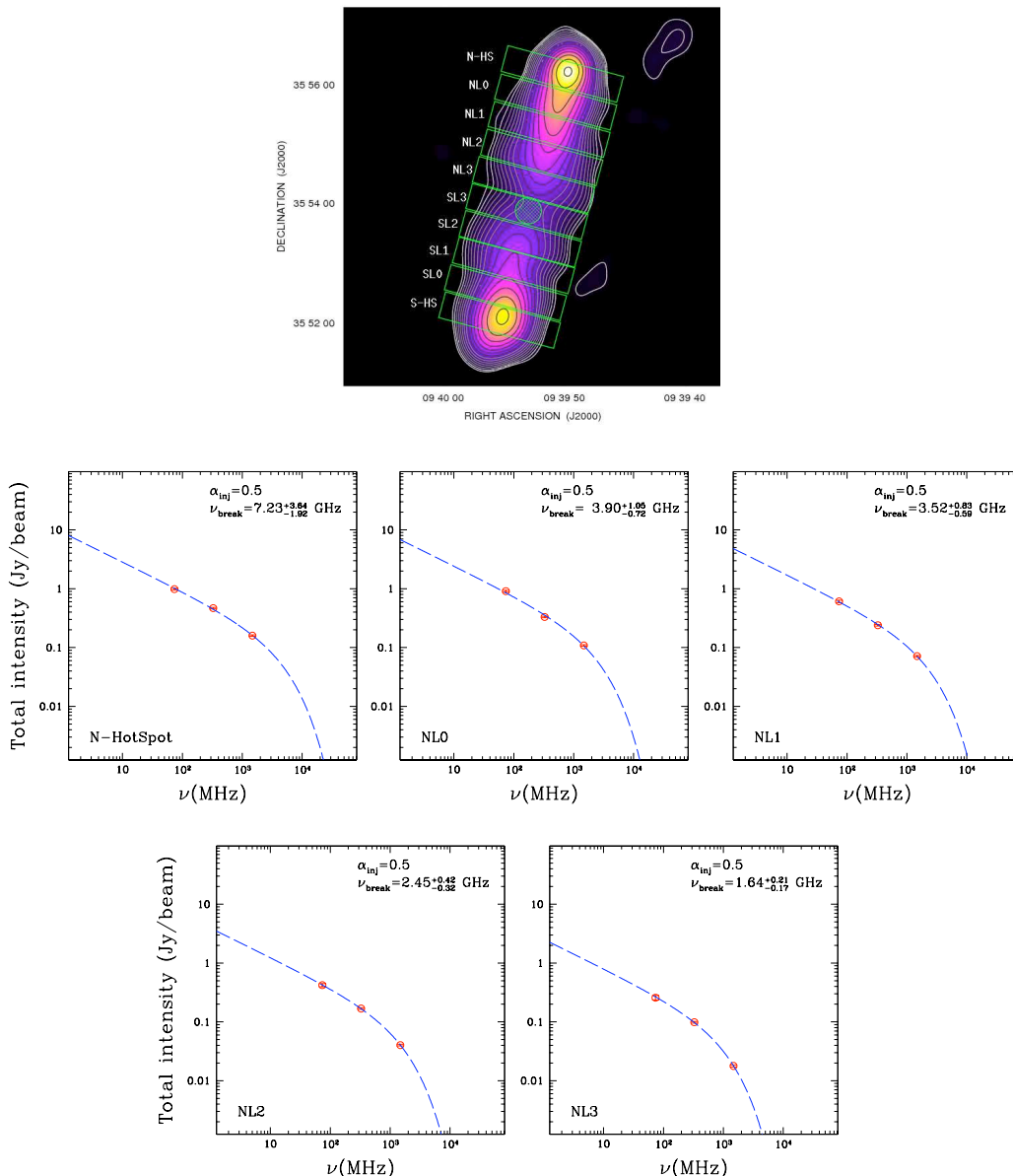


**Fig. 6. a.** 3C223: Color map of the source (resolution  $26''$ ) and the contours at 327 MHz ; overlaid the green array of boxes where the measures have been taken. For the N lobe: plots represent the spectral shape of the source labeled according to the positions. Points are measures taken at three frequencies, dashed lines are the fits with the synchrotron model.

For the radio galaxy 3C223, the spectral index distribution between 74 and 327 MHz ( $26'' \times 26''$ ) is slightly more patchy than that of 3C35. The average value of  $\alpha$  is about  $0.60 \pm 0.03$ . In the North hot spot the spectral index reaches values of  $\sim 0.40 \pm 0.01$ , while in the low brightness regions of the lobes the spectral index steepens up to  $\alpha \sim 1.67 \pm 0.02$ .

The spectral index map between 327 MHz and 1.48 GHz ( $7.5'' \times 7.5''$ ) for 3C223 shows that the spectral index increases from  $\alpha \sim 0.72 \pm 0.01$  in the region of the head of the lobes, up to values of  $\alpha \sim 1.32 \pm 0.09$  in the inner regions of the lobes near to the core. The image used at 1.48 GHz was made from VLA archive data (Leahy & Perley 1991).

### 3.4. Measure and estimate of physical parameters

For both sources the flux density at 74 and 327 MHz was measured in the same regions. The values listed in Table 4 and Table 5 indicate the flux of the entire source, of the two lobes separately and of the core when detected. For these regions we also calculated the spectral index between 74 and 327 MHz and the equipartition magnetic field (Tables 4 and 5). The measured total flux densities at 327 MHz have been compared with the measurements of the WENSS, these are in agreement within the errors for both sources.

The zero-order estimate of the magnetic field strength, averaged over the entire source volume, can be derived under the assumption of classical equipartition. Here, the radio source is in a minimum energy condition and the relativistic particle energy density equals the magnetic field energy density. In the framework



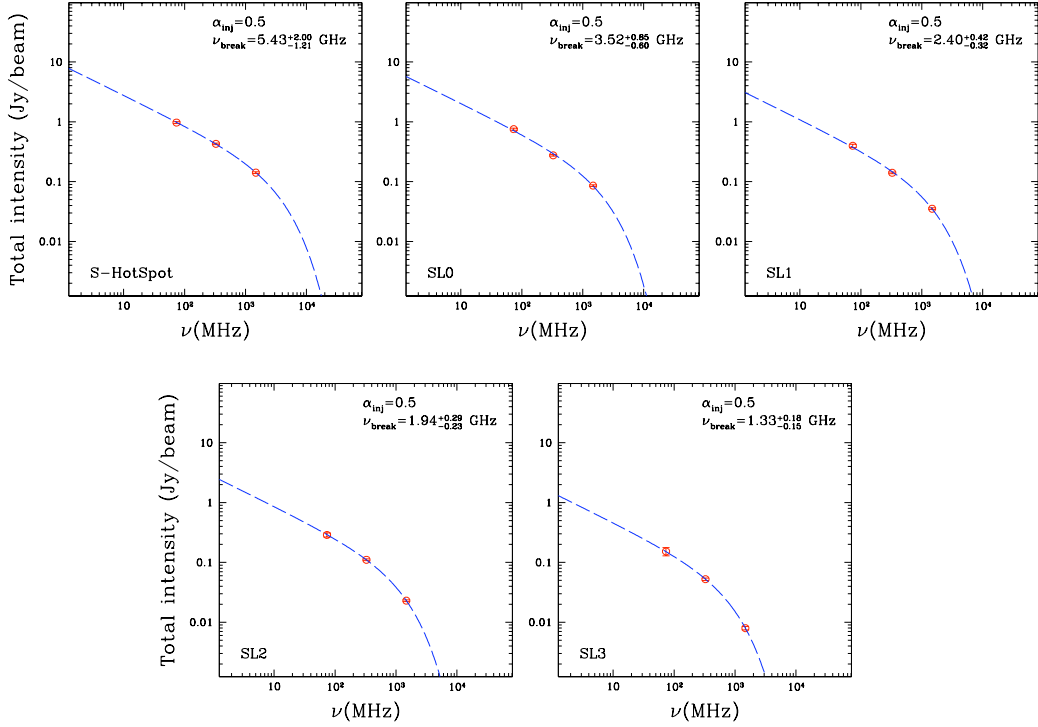


**Fig. 6. b.** Similar to Fig.6 for the the S lobe of 3C223

**Table 3.** Resolution and rms of the images used for the spectral index maps.

name	$\nu$ MHz	resolution "x"	rms mJy/beam
3C35	74	95×95	92.4
	327	95×95	7.0
	327	45×45	2.1
	1400	45×45	0.5
3C223	74	26×26	43.6
	327	26×26	3.5
	327	7.5×7.5	0.7
	1480	7.5×7.5	0.1

of the equipartition hypothesis, the magnetic field can be determined from the radio synchrotron luminosity and the source volume. We estimated the equipartition magnetic field assuming a magnetic field entirely filling the radio source in a range of frequencies in which the synchrotron luminosity is calculated from a low frequency cutoff of 10 MHz to a high frequency cutoff of 10 GHz. The volume averaged magnetic fields were evaluated within a cylinder. Then we considered two cases: a) one in which the energy is equally divided between relativistic protons and electrons–positrons, and the ratio between protons and electrons  $k=p/e$  will be  $k=1$ , and b) one case in which all the energy is provided by a plasma of relativistic electrons–positrons and  $k=0$ .

In our case we consider a power-law injection spectrum with index  $\delta$ , therefore, since  $\alpha = (\delta - 1)/2$ , we adopted the measured spectral index  $\alpha$  for the estimate of the magnetic field.

**Table 4.** 3C35 Flux densities, spectral indices and equipartition magnetic fields.

	Total	N lobe	S lobe	Core
$F_{73.8\text{MHz}}(\text{Jy})$	$20.9 \pm 0.7$	$10.8 \pm 0.4$	$10.2 \pm 0.5$	
$F_{327.4\text{MHz}}(\text{Jy})$	$7.5 \pm 0.2$	$3.9 \pm 0.1$	$3.6 \pm 0.1$	$0.171 \pm 0.004$
$\alpha_{74}^{327}$	0.7	0.7	0.7	
$B_{eq-\gamma}(\mu\text{G})$	0.72	0.73	0.71	$k=1$
	0.59	0.59	0.58	$k=0$
$B_{eq-\gamma}(\mu\text{G})$	1.03	1.04	1.02	$k=1$
	0.85	0.86	0.84	$k=0$

Assuming a low-frequency cut-off of 10 MHz in the luminosity calculation is equivalent to assuming a low-energy cut-off of  $\gamma_{min} \sim 2000$  in the particle energy spectrum ( $B_{eq-\gamma}$  in Tables 4 and 5). Therefore, in our estimates of  $B_{eq}$  we adopted the revised formalism (Brunetti et al. 1997, Beck & Krause 2005) assuming a low-energy cut-off of  $\gamma_{min} = 100$  in the particle energy distribution rather than a low-frequency cut-off in the emitted synchrotron spectrum ( $B_{eq-\gamma}$  in Tables 4 and 5).

For 3C35 we considered a cylinder of 190 kpc of radius and height  $\sim 1$  Mpc. The adopted spectral index of the electron energy spectrum, between 74 and 327 MHz (Table 4) is  $\alpha \simeq 0.7$ , which yields  $\delta = 2.4$ . The volume of the two lobes respectively is one half of the total volume. The measure of the fluxes includes the emission of the hot-spots. The estimated equipartition magnetic field strength values are listed in Table 4.

For the radio source 3C223, we assumed a cylinder with radius of  $\sim 200$  kpc and height  $\sim 900$  kpc. The spectral index of the

**Table 5.** 3C223 Flux densities, spectral indices and equipartition magnetic fields.

	Total	N lobe	S lobe	Core
$F_{73.8\text{MHz}}(\text{Jy})$	$30.2 \pm 1.0$	$16.2 \pm 0.6$	$14.0 \pm 0.5$	
$F_{327.3\text{MHz}}(\text{Jy})$	$11.7 \pm 0.4$	$6.4 \pm 0.2$	$5.2 \pm 0.2$	$0.031 \pm 0.002$
$\alpha_{74}^{327}$	0.6	0.6	0.7	
$B_{eq-\nu}(\mu\text{G})$	1.28 1.05	1.31 1.07	1.26 1.03	k=1 k=0
$B_{eq-\gamma}(\mu\text{G})$	1.58 1.31	1.62 1.34	1.75 1.45	k=1 k=0

electron energy spectrum of the entire source and of the North lobe is  $\delta = 2.2$  which corresponds to  $\alpha_{74}^{327} \approx 0.6$ , while for the South lobe we used  $\delta = 2.4$  which corresponds to  $\alpha_{74}^{327} \approx 0.7$ . The contribution of the hot-spot emission was included in these measures. The resulting equipartition magnetic fields strength are presented in Table 5.

One of the most important physical properties of GRG, which distinguish them from compact and powerful sources like e.g. CygA, is that the equipartition magnetic field is far below the inverse Compton equivalent field over most of the lobes (see Tab. 4 & 5). This means that the electron energy losses are largely dominated by the inverse Compton scattering of the CMB photons, which can be assumed fairly uniform and isotropic. Thus, the location of the break energy is mostly unaffected by eventual gradients of the magnetic field in the lobe. However, very strong negative magnetic field gradients from the hot-spot to the core, if any, could affect the location of the break frequency and mimic the effect of aging, i.e. the source would appear older than what really is. Although, at least in the case of 3C223, we know from the X-ray data that the equipartition magnetic field is correct to within a factor of 2. However, in the hot-spots the situation is different and the magnetic field could be significantly higher than  $B_{IC}$ , where  $B_{IC}$  is the magnetic field directly estimated by using X-ray and radio data. On the other hand, in this regions radiative losses are balanced by re-acceleration and injection of new particles to form what we define as "the zero-age injection spectrum" (see the discussion in Carilli et al. 1991). Unfortunately, we do not have enough resolution in our images to resolve the hot-spots in our GRGs and thus to address this issue further in details.

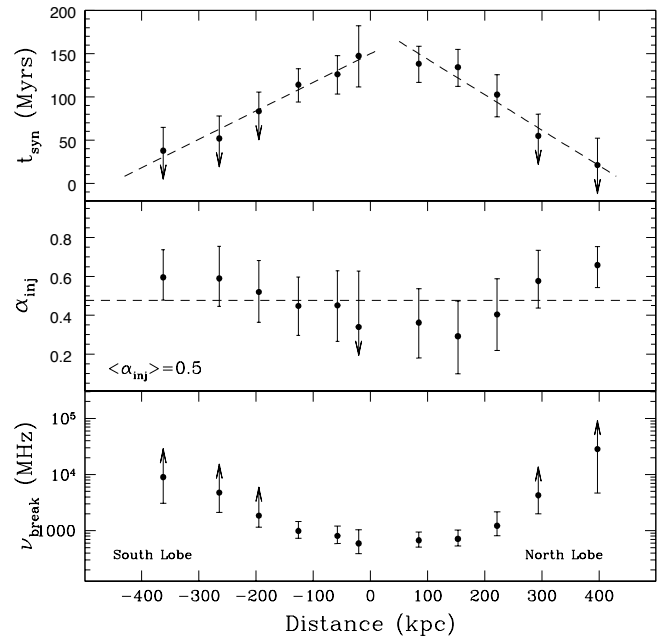
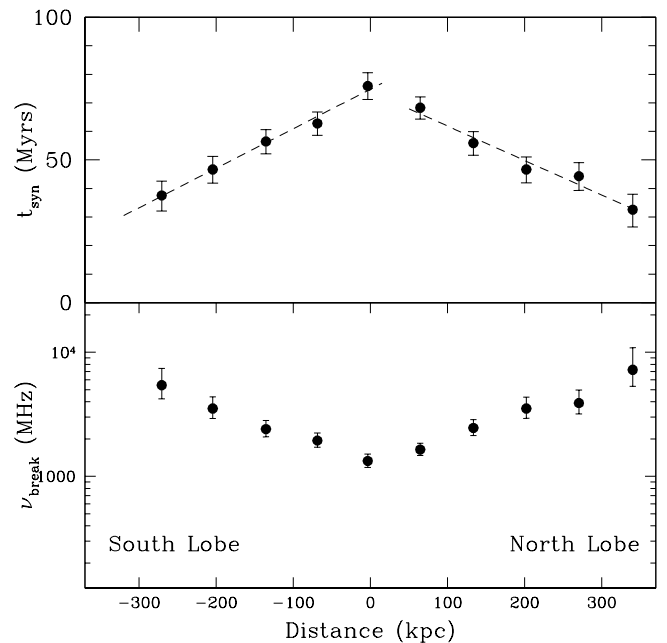
## 4. Synchrotron Model

### 4.1. Fitting the spectral shape

The extended size of the two sources and the resolution reached in our images allowed us to describe at different frequencies the variation of the total intensity, from the hot-spot, where the particles are injected, up to the inner regions of lobes, where the older less energetic electrons are supposed to be located. We assumed that the particles are injected by the jets in the intergalactic medium, in a certain epoch  $t_0$ , with a power-law energy spectrum:

$$N(\varepsilon) \propto N_0 \varepsilon^{-\delta_{inj}}; \quad (1)$$

then the jets move further injecting particles in another region. This continues up to the hot spots where particles are injected at

**Fig. 7.** 3C35: plotted with respect to the distance from the core: the fitted values of  $\nu_{break}$  (bottom); the fitted values for  $\alpha_{inj}$  (center); the estimated synchrotron ages (top).**Fig. 8.** 3C223: plotted with respect to the distance from the core: the fitted values of  $\nu_{break}$  (bottom) and the estimated synchrotron ages (top).

the current epoch. The relativistic particles emit a synchrotron radiation and the spectrum is still a power-law with a spectral index  $\alpha_{inj} = (\delta_{inj} - 1)/2$ . Particles are affected by radiative losses via synchrotron and inverse Compton processes, therefore the

radio spectrum moves away from the original power-law with a break at high frequencies.

The JP model (Jaffe & Perola 1973) was used in this analysis. In this model the pitch angle scattering is very efficient; indeed the isotropization occurs on a time scale much shorter than the radiative time-scale. Because the pitch angle is continuously randomized, each particle of the electron population can assume all possible orientations with respect to the magnetic field. In the framework of the JP model, the break frequency  $\nu_{break}$  is a time-dependent function, that can be estimated by fitting the curvature of the radio spectra. If there is no expansion and the magnetic field is constant, the break frequency depends on the elapsed time since the injection of the particles according to this formula (Slee et al. 2001):

$$t_{syn} = 1590 \frac{B_{eq}^{1/2}}{(B_{eq}^2 + B_{CMB}^2)} \frac{1}{[\nu_{break}(1+z)]^{1/2}} \text{ Myrs} \quad (2)$$

where  $t_{syn}$  is the radiative age of the source,  $\nu_{break}$  is measured in GHz,  $B_{eq}$  and  $B_{CMB} = 3.25(1+z)^2$  are the equipartition and inverse Compton equivalent magnetic fields respectively, both measured in  $\mu\text{G}$ .

For each source we measured the total intensity for the N lobe and S lobe in a grid of boxes placed along the source (top panels of the Figures 5a and 6a). For the source 3C35 we choose the size of the boxes of half of the beam size for the lobes in order to have an even number of nearly independent measures, this fine sampling does not affect the age estimate. Since the poor resolution, to avoid the breaking off of the hot-spots in two boxes, the boxes of the two hot-spots have been selected of about one beam size. For the source 3C223 boxes are about one beam size.

The plots in the figures 5a and 6a refer to the N lobes while the 5b and 6b show the S lobes respectively of the sources 3C35 and 3C223. The contribution of the emission from the core has been masked for both sources. Each plot corresponds to a box as shown in the labels on the bottom-left corner. The red dots represent the data, while the blue dashed lines are the fit with the model.

The model used to fit the data is the JP model available in the software package Synage++ (Murgia 2000). For these two radio sources, the choice of the JP model is justified by the fact that since the magnetic field is low, the inverse Compton losses are as important as synchrotron losses, therefore the CMB isotropises the electron population.

The spectra of 3C35 have been obtained using cube images with frequencies of 74, 327, 608 and 1400 MHz at the resolution of  $95''$ . To perform this analysis we used the 608 MHz WSRT image with a resolution of  $40'' \times 20''$ , PA= $0^\circ$  and rms 1.3 mJy/beam; the 1.4 GHz image has been taken from the NVSS. The free parameters in the fit are: the break frequency  $\nu_{break}$ , the injection spectral index  $\alpha_{inj}$  and the flux normalization, which is proportional to the integral along the line of sight of the product  $N_0 \times B^{1+\alpha}$ . The resulting fitted parameters obtained for each box and the reduced  $\chi^2$  ( $\chi^2/\text{ndf}$ , where ndf is the number of degrees of freedom) are listed in Tab.6. The shape of the hot spots are well described by power-laws; the estimated break frequencies are  $>4.71$  GHz for the North hot spot and  $>3.07$  GHz for the South. The injection spectral index is  $0.66^{+0.09}_{-0.12}$  and  $0.59^{+0.14}_{-0.12}$  for the North and for the South hot spots respectively. In the inner part of the lobes  $\nu_{break}$  is  $\approx 700\text{-}800$  MHz. The fitted spectra are plotted in Fig.5a and 5b and summarized in Fig.7 as a function of the distance from the core. The central panel of Fig.7 shows a variation of the injection spectral index along the source, the values range from 0.29 to 0.66; on average  $\langle \alpha_{inj} \rangle \approx 0.5$ . A vari-

able spectral index could be explained in terms of deceleration of the relativistic plasma along the jets, following the subsequently happening of multiple shocks (Meli et al. 2008). This could be observed with a steepening of the electron spectra and in parallel of  $\alpha_{inj}$  with the aging of the source. Observations of the electron spectra from the terminal hot-spots to the lobes of the powerful FR-II radio galaxies showed that these have not a single and universal power-law form (Rudnick et al. 1994; Machalski et al. 2007).

Nevertheless, it should be considered that our error bars on  $\alpha_{inj}$  are large, and hence the injection spectral index could still be considered fairly constant around a value of  $\approx 0.5$ . Future observations at possibly higher sensitivity are needed to confirm the  $\alpha_{inj}$  trend along the lobes definitely.

The top panel of Fig.7 shows the synchrotron age of 3C35 calculated by using the formula 2. The values used for  $\nu_{break}$  and  $B_{eq}$  ( $k=1$ ) are listed respectively in Tab. 6 and 4. The synchrotron age calculated for the source 3C35 is  $138^{+20}_{-22}$  Myr for the North lobe and  $147^{+35}_{-36}$  Myr for the South lobe. Therefore, in agreement with Parma et al. (1999), 3C35 can be considered an old source. Moreover, since from the plot we can see that the  $t_{syn}$  increases linearly with the distance from the hot-spots, we can conclude that the source reached this size expanding with a constant velocity in the extragalactic medium  $v_{exp} \sim 0.011c$ .

In the analysis of 3C223 we used images at 74, 327 and 1400 MHz with a resolution of  $26''$ . The 1.4 GHz image is from Leahy & Perley (1991). We used a fixed  $\alpha_{inj} = 0.5$ , assumed according to the literature, because the observational data were only for three frequencies, which restricts to two the number of free parameters. The free parameters in this case are the break frequency  $\nu_{break}$  and the flux normalization. The resulting fitted parameters obtained for each box and the reduced  $\chi^2$  are listed in Tab. 7. In this case the spectral shape and the of the hot spots drifts away from a power-law, a  $\nu_{break}$  of about 6.0-7.0 GHz has been estimated. In the inner regions of the lobes the spectrum steepens and the  $\nu_{break}$  is  $\approx 1.5$  GHz. The fitted spectra are plotted in Fig.6a and 6b and summarized as function of the distance from the core in Fig.8.

In the top panel of Fig.8 we plot the synchrotron age of 3C223 estimated from the formula 2, and using the values of  $\nu_{break}$  and  $B_{eq}$  in Tab. 7 and 5. For the source 3C223 the  $t_{syn}$  is  $68^{+4}_{-4}$  for the North lobe and  $76^{+5}_{-5}$  Myr for the South lobe. As for 3C35, the age decreases linearly with the distance from the core, so we can assume that the lobes advanced with a constant velocity  $v_{exp} \sim 0.017c$ .

The 5 GHz archival data were not included in the spectral aging analysis since the low-surface brightness emission near the core is not properly imaged by the interferometric observations at 5 GHz due to the lack of short-space baselines. However, it should be noted that the fit of the JP model is able to recover also a break frequency significantly above the maximum frequency in our data set since the spectral shape departs from a pure power law well before  $\nu_{break}$ . In fact, although in the JP model all particles have the same break energy, the break frequency of the particles at small pitch angle,  $\theta$ , is also smaller:  $\nu_{break}(\theta) \propto \sin\theta$ .

#### 4.2. Fit of the spectral index profile

In this section we evaluate, independently for the two lobes of each source, the frequency break and the injection spectral index, by fitting with the synchrotron model the two frequency spectral index,  $\alpha_{1.4}^{0.3}$  as a function of the distance from the core. This method allows an investigation of the spectral index behaviour

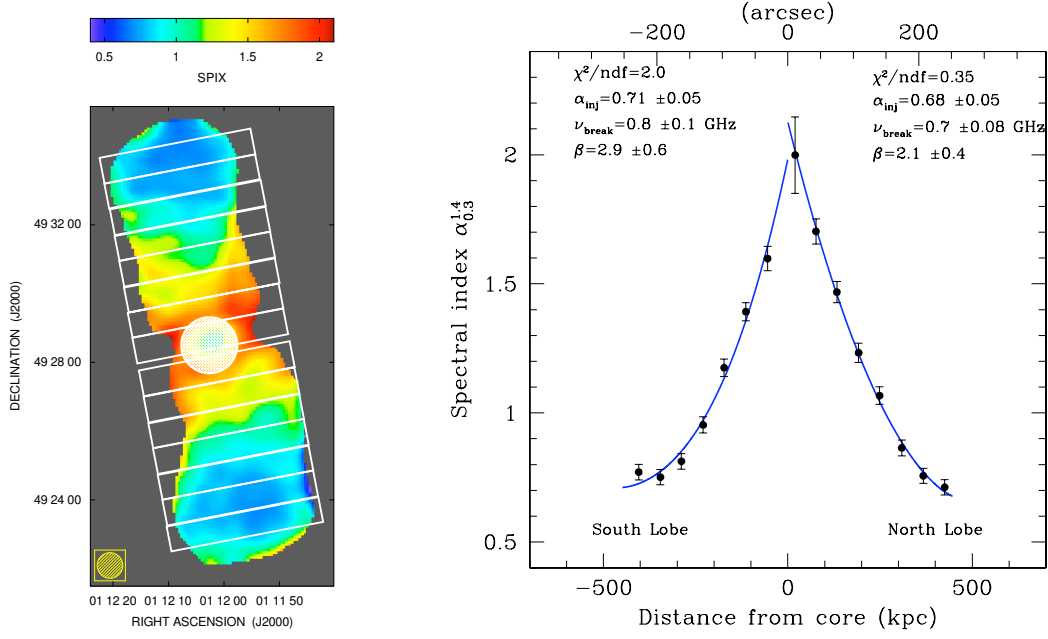


**Fig. 9.** 3C35: *left* in color the spectral index map between 327 MHz and 1.4 GHz; overlaid the white array of boxes where the measures have been taken. *Right* fit of the spectral index  $\alpha_{1.4}^{0.3}$  with the synchrotron model.

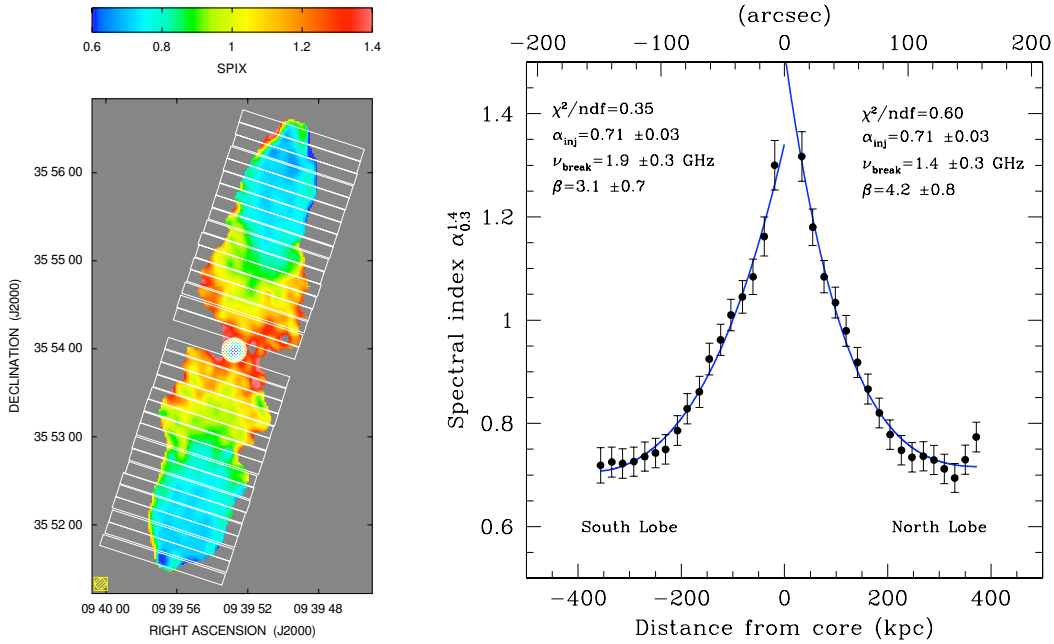


**Fig. 10.** 3C223: *left* in color the spectral index map between 327 MHz and 1.48 GHz; overlaid the white array of boxes where the measures have been taken. *Right* fit of the spectral index  $\alpha_{1.4}^{0.3}$  with the synchrotron model.

at higher spatial resolution than we used in the previously described, multi-frequency analysis (Sect. 4.1), which was limited by the resolution of the 74 MHz images. Following the assumption that the sources are expanding with a constant velocity, we have that  $\nu_{break} \propto 1/t^2 \propto 1/d^2$  since  $t=d/v$ . Here  $t$  is the age and  $d$  is the distance from the hot-spot. We fitted  $\nu_{break} \propto 1/d^\beta$ , where  $\beta$  is a free parameter. If  $\beta$  is 2, this means that the source is expanding with a constant velocity and adiabatic losses are negligible. If  $\beta$  is steeper than 2 either the expansion losses play

an important role in the energetic of the source and/or the radio source is not expanding with a constant speed.

The fit for the source 3C35 (Fig.9) gives  $\nu_{break} \approx 0.7$ - $0.8$  GHz which is in good agreement with the one found in Sect.4.1.  $\alpha_{inj}=0.7$  is slightly steeper with respect to the  $\alpha_{inj}$  found in Sect.4.1, but still consistent within the errors. For this source the value of the parameter  $\beta$  is close to a value of about  $2.5 \pm 0.7$  this means that adiabatic losses are negligible for 3C35, this can be further confirmed by the tubular structure of the source.

**Table 6.** 3C35: break frequency, alpha injection and reduced  $\chi^2$ .

Region	$\nu_{break}$ GHz	$\alpha_{inj}$	$\chi^2_{red.}$
N-HotSpot	> 4.71	0.66 <sup>+0.09</sup> <sub>-0.12</sub>	0.3
NL0	4.27 <sup>+29.86</sup> <sub>-2.26</sub>	0.58 <sup>+0.16</sup> <sub>-0.14</sub>	0.01
NL1	1.23 <sup>+0.41</sup> <sub>-0.41</sub>	0.40 <sup>+0.18</sup> <sub>-0.18</sub>	0.5
NL2	0.72 <sup>+0.31</sup> <sub>-0.18</sub>	0.29 <sup>+0.18</sup> <sub>-0.19</sub>	0.6
NL3	0.67 <sup>+0.27</sup> <sub>-0.16</sub>	0.36 <sup>+0.17</sup> <sub>-0.18</sub>	2.8
C0	0.59 <sup>+0.44</sup> <sub>-0.21</sub>	0.34 <sup>+0.29</sup> <sub>-0.34</sub>	4.2
SL3	0.81 <sup>+0.40</sup> <sub>-0.22</sub>	0.45 <sup>+0.18</sup> <sub>-0.19</sub>	1.4
SL2	0.99 <sup>+0.46</sup> <sub>-0.26</sub>	0.45 <sup>+0.15</sup> <sub>-0.15</sub>	0.2
SL1	1.85 <sup>+2.08</sup> <sub>-0.69</sub>	0.52 <sup>+0.16</sup> <sub>-0.16</sub>	0.05
SL0	4.77 <sup>+60.00</sup> <sub>-2.66</sub>	0.59 <sup>+0.17</sup> <sub>-0.14</sub>	0.01
S-HotSpot	> 3.07	0.59 <sup>+0.14</sup> <sub>-0.12</sub>	0.2

**Table 7.** 3C223: break frequency and reduced  $\chi^2$ .

Region	$\nu_{break}$ GHz	$\chi^2_{red.}$
N-HotSpot	7.23 <sup>+3.64</sup> <sub>-1.92</sub>	1.3
NL0	3.90 <sup>+1.05</sup> <sub>-0.72</sub>	4.0
NL1	3.52 <sup>+0.83</sup> <sub>-0.59</sub>	0.5
NL2	2.45 <sup>+0.42</sup> <sub>-0.32</sub>	0.05
NL3	1.64 <sup>+0.21</sup> <sub>-0.17</sub>	0.2
SL3	1.33 <sup>+0.18</sup> <sub>-0.15</sub>	0.01
SL2	1.94 <sup>+0.29</sup> <sub>-0.23</sub>	0.03
SL1	2.40 <sup>+0.42</sup> <sub>-0.32</sub>	1.6
SL0	3.52 <sup>+0.85</sup> <sub>-0.60</sub>	3.2
S-HotSpot	5.43 <sup>+2.00</sup> <sub>-1.21</sub>	0.1

For the source 3C223 (Fig.10) we found  $\nu_{break} \approx 1.4 - 1.9$  GHz, which is consistent with the one found fitting the spectral shape in Sect. 4.1. In this case the injection index of 0.71 is steeper than the assumed  $\alpha_{inj}=0.5$  used previously (Sect. 4.1) and probably reflects both the higher frequency range of this method and the non-power-law shape of the hot-spots in this source. The parameter  $\beta$  for this source is about  $3.6 \pm 1.1$ . As noted above,  $\beta > 2$  indicates either expansion energy losses or a source expanding at a non-constant speed. A physical motivation for such a value could be explained as follows. If the inverse Compton dominates the radiative losses,  $\epsilon_{break} \propto 1/t$  while  $\nu_{break} \propto B \cdot \epsilon_{break}^2$ , where  $\epsilon_{break}$  is the energy break and  $B$  is the magnetic field. The magnetic field decreases with the lateral expansion of the lobes as  $B \propto 1/R^2$ , where  $R$  is the radius of section of the lobe. Since the source evolves in a self-similar way (Kaiser & Alexander 1997),  $R$  is proportional to  $d$ , which gives  $B \propto 1/d^2$ , and therefore  $\nu_{break} \propto 1/d^4$ . That is the value that we found for the free parameter  $\beta$ . In this case the action of expansion losses can be seen in the arrow structure of the source.

## 5. Summary and conclusions

In this paper we present new VLA images of the sources 3C35 and 3C223 at the observing frequencies of 327 and 74 MHz.

By combining our images with those at 1.4 GHz available in the literature, we produced spectral index distribution maps between 74–327 MHz and 327 MHz–1.4 GHz for both sources. The spectral index across the sources are more constant in the

low frequency range, while in the high frequency range the spectral indices increase from the hot-spots to the inner region of the lobes near to the core. In particular, for the source 3C35,  $\alpha$  ranges between 0.6 and 0.8 in the interval of frequencies 74–327 MHz, while between the frequencies 327 MHz–1.4 GHz the values of  $\alpha$  change from 0.6 in the hot-spot's region to 1.7 in the inner region of the lobes. On the other hand, for the source 3C223 the value of  $\alpha$  is on average 0.6 in the range 74–327 MHz, but it could reach extreme values which range between 0.4 and 1.6. In the range between 327 MHz–1.4 GHz  $\alpha$  varies from 0.7 in the hot-spots to 1.5 in the inner region of the lobes.

By considering the two radio sources in a minimum energy condition, i.e. in the equipartition regime, we estimated the magnetic field of the two sources. The estimate was made using two different approaches often adopted in the literature, a fixed frequency range and a fixed energy range. Moreover, two different plasma populations has been considered (see Tab. 4 and 5): one in which the energy is equally divided between relativistic protons and electrons and another one in which all the energy is provided by a plasma of relativistic electrons–positrons. For both sources the resulting equipartition magnetic field ranges between values of 0.5–1.6  $\mu$ G, in concordance with typical values of the measured IC magnetic fields. In particular, in the case of 3C223, the value of the equipartition magnetic field is within a factor of two in agreement with the measured IC magnetic field (Croston et al. 2004).

By using our images with those at higher frequencies available in the literature, we obtained the spectral shape of the radio spectrum in many different positions along the lobes. The hot spots of the source 3C35 are well described by power-laws, while the hot spots of 3C223 show quite curved spectra. The inner regions of the lobes for the two sources present a break in the range of frequency around 1.0 GHz.

Since for both the sources the magnetic field is low, the inverse Compton losses are as important as the synchrotron losses, and we can assume an isotropic electron population. Therefore we fitted the spectra with a JP (Jaffe & Perola 1973) model to estimate the frequency break  $\nu_{break}$ ; in the case of 3C35 we also estimated  $\alpha_{inj}$  while for 3C223 we used a fixed value. In the case of 3C35 we found that  $\nu_{break} \approx 800$  MHz and  $\alpha_{inj}$  is on average 0.5. For 3C223 the  $\nu_{break}$  is about 1.4 GHz with a fixed  $\alpha_{inj}=0.5$ .

The break frequency  $\nu_{break}$  is a time-dependent function, by assuming that there is no expansion and the magnetic field is constant, from the frequency break we calculated the radiative age of the source  $t_{syn}$ . Blundell & Rawlings (2000) claimed an anomalous diffusion of relativistic particles which implies that no information about the age of the source can be inferred from the shape of the emission radio spectrum. They discussed about the discrepancy between the estimates of the spectral and dynamical ages for sources older than  $10^7$  yr. But Kaiser (2000) demonstrated that diffusion will not alter the distribution of relativistic particles, therefore the spatial distribution of the synchrotron radio emission can be used to estimate the age for FR II sources (Fanaroff & Riley 1974). Moreover, as we discussed above, the magnetic field of these particular sources is low with respect to the inverse Compton equivalent magnetic field, therefore a spatially variable magnetic field has a minor impact on the energy losses of the relativistic electrons. For 3C35 the estimated age is about  $143 \pm 20$  Myr while for 3C223 is about  $72 \pm 4$  Myr. The radiative age confirms that the two sources are rather old. However, these estimates must be considered upper limits if adiabatic losses can not be neglected.

A high resolution analysis of the spectral index behaviour has been made by fitting the two frequency spectral index  $\alpha_{1.4}^{0.3}$

with the synchrotron model as function of the distance from the core. We fitted with a law  $\nu_{break} \propto 1/d^\beta$ . For the source 3C35 the frequency break is about 800 MHz and parameter  $\beta$  is about  $2.5 \pm 0.7$ , in agreement with an expansion with a constant speed and/or unimportant adiabatic losses. For the source 3C223,  $\nu_{break} \approx 1.4$  GHz, while the parameter  $\beta$  is about  $3.6 \pm 1.1$ ; as discussed before this could be explained if adiabatic losses play an important role in the energy balance of the source and/or if the expansion velocity of the source is not constant.

*Acknowledgements.* We would like to thank the anonymous referee for insightful comments which improved this manuscript. E.O. acknowledges financial support of Austrian Science Foundation (FWF) through grant number P18523-N16. The National Radio Astronomy Observatory is operated by Associated Universities, Inc., under contract to the National Science Foundation. This research has made use of the NASA/IPAC Extragalactic Database (NED) which operated by the Jet Propulsion Laboratory, California Institute of Technology, under contract with the National Aeronautics and Space Administration and of CATS database Astrophysical CATalogs support System.

## References

- Abazajian, K. N., Adelman-McCarthy, J. K., Agüeros, M. A., et al. 2009, *ApJS*, 182, 543
- Baum, S. A., Heckman, T. M., Bridle, A., van Breugel, W. J. M., & Miley, G. K. 1988, *ApJS*, 68, 643
- Beck, R. & Krause, M. 2005, *Astronomische Nachrichten*, 326, 414
- Begelman, M. C., Blandford, R. D., & Rees, M. J. 1984, *Reviews of Modern Physics*, 56, 255
- Blandford, R. D. & Rees, M. J. 1974, *MNRAS*, 169, 395
- Blundell, K. M. & Rawlings, S. 2000, *AJ*, 119, 1111
- Blundell, K. M., Rawlings, S., & Willott, C. J. 1999, *AJ*, 117, 677
- Brunetti, G., Setti, G., & Comastri, A. 1997, *A&A*, 325, 898
- Burbidge, E. M. & Strittmatter, P. A. 1972, *ApJ*, 172, L37+
- Carilli, C. L., Perley, R. A., Dreher, J. W., & Leahy, J. P. 1991, *ApJ*, 383, 554
- Cohen, A. S., Lane, W. M., Cotton, W. D., et al. 2007, *AJ*, 134, 1245
- Condon, J. J., Cotton, W. D., Greisen, E. W., et al. 1998, *AJ*, 115, 1693
- Cornwell, T. J. & Perley, R. A. 1992, *A&A*, 261, 353
- Cotton, W. D., Condon, J. J., Perley, R. A., et al. 2004, in *Ground-based Telescopes*. Edited by Oschmann, Jacobus M., Jr. *Proceedings of the SPIE*, Volume 5489, pp. 180-189 (2004), ed. J. M. Oschmann, Jr., 180–189
- Croston, J. H., Birkinshaw, M., Hardcastle, M. J., & Worrall, D. M. 2004, *MNRAS*, 353, 879
- Croston, J. H., Hardcastle, M. J., Harris, D. E., et al. 2005, *ApJ*, 626, 733
- Eilek, J. A., Melrose, D. B., & Walker, M. A. 1997, *ApJ*, 483, 282
- Fanaroff, B. L. & Riley, J. M. 1974, *MNRAS*, 167, 31P
- Goodger, J. L., Hardcastle, M. J., Croston, J. H., Kassim, N. E., & Perley, R. A. 2008, *MNRAS*, 386, 337
- Hardcastle, M. J. & Croston, J. H. 2005, *MNRAS*, 363, 649
- Hogbom, J. A. 1979, *A&AS*, 36, 173
- Ishwara-Chandra, C. H. & Saikia, D. J. 1999, *MNRAS*, 309, 100
- Isoke, N., Tashiro, M., Makishima, K., et al. 2002, *ApJ*, 580, L111
- Jaffe, W. J. & Perola, G. C. 1973, *A&A*, 26, 423
- Jägers, W. J. 1987, *A&AS*, 67, 395
- Jamrozy, M., Klein, U., Mack, K.-H., Gregorini, L., & Parma, P. 2004, *A&A*, 427, 79
- Jamrozy, M., Konar, C., Machalski, J., & Saikia, D. J. 2008, *MNRAS*, 385, 1286
- Jamrozy, M., Machalski, J., Mack, K.-H., & Klein, U. 2005, *A&A*, 433, 467
- Kaiser, C. R. 2000, *A&A*, 362, 447
- Kaiser, C. R. & Alexander, P. 1997, *MNRAS*, 286, 215
- Kaiser, C. R., Dennett-Thorpe, J., & Alexander, P. 1997, *MNRAS*, 292, 723
- Kardashev, N. S. 1962, *Soviet Astronomy*, 6, 317
- Kassim, N. E., Lazio, T. J. W., Erickson, W. C., et al. 2007, *ApJS*, 172, 686
- Kassim, N. E., Perley, R. A., Erickson, W. C., & Dwarakanath, K. S. 1993, *AJ*, 106, 2218
- Kellermann, K. I. 1964, *ApJ*, 140, 969
- Konar, C., Hardcastle, M. J., Croston, J. H., & Saikia, D. J. 2009, *MNRAS*, 400, 480
- Laing, R. A. & Peacock, J. A. 1980, *MNRAS*, 190, 903
- Laing, R. A., Riley, J. M., & Longair, M. S. 1983, *MNRAS*, 204, 151
- Lane, W. M., Cohen, A. S., Kassim, N. E., et al. 2005, *Radio Science*, 40, 5
- Lara, L., Giovannini, G., Cotton, W. D., et al. 2004, *A&A*, 421, 899
- Leahy, J. P. & Perley, R. A. 1991, *AJ*, 102, 537
- Machalski, J., Chyży, K. T., Stawarz, Ł., & Koziel, D. 2007, *A&A*, 462, 43
- Mason, K. O., Carrera, F. J., Hasinger, G., et al. 2000, *MNRAS*, 311, 456
- Meli, A., Becker, J. K., & Quenby, J. J. 2008, *A&A*, 492, 323
- Murgia, M., 2000, PhD Thesis, University of Bologna
- Pacholczyk, A. G. 1970, *Radio astrophysics. Nonthermal processes in galactic and extragalactic sources* (Series of Books in Astronomy and Astrophysics, San Francisco: Freeman, 1970)
- Parma, P., Murgia, M., Morganti, R., et al. 1999, *A&A*, 344, 7
- Perley, R. A. 1999, in *ASP Conf. Ser. 180: Synthesis Imaging in Radio Astronomy II*, ed. G. B. Taylor, C. L. Carilli, & R. A. Perley, 383
- Rengelink, R. B., Tang, Y., de Bruyn, A. G., et al. 1997, *A&AS*, 124, 259
- Rudnick, L., Katz-Stone, D. M., & Anderson, M. C. 1994, *ApJS*, 90, 955
- Saripalli, L., Hunstead, R. W., Subrahmanyan, R., & Boyce, E. 2005, *AJ*, 130, 896
- Scheuer, P. A. G. 1974, *MNRAS*, 166, 513
- Schoenmakers, A. P., de Bruyn, A. G., Röttgering, H. J. A., & van der Laan, H. 2001, *A&A*, 374, 861
- Schoenmakers, A. P., Mack, K.-H., de Bruyn, A. G., et al. 2000, *A&AS*, 146, 293
- Slee, O. B., Roy, A. L., Murgia, M., Andernach, H., & Ehle, M. 2001, *AJ*, 122, 1172
- Spergel, D. N., Verde, L., Peiris, H. V., et al. 2003, *ApJS*, 148, 175
- Tribble, P. C. 1993, *MNRAS*, 261, 57
- van Breugel, W. & Jägers, W. 1982, *A&AS*, 49, 529

## Appendix A: Faint radio galaxy

In the field of 3C223 at 327 MHz, at the position RA  $09^h 40^m 13.9^s$  Dec  $+35^\circ 57' 34''$ , we detected a small double-lobed radio source. This radio source has already been detected (see Fig. 6 in Croston et al. (2004)) in the 1.4 GHz VLA data by Leahy & Perley (1991). In the same position, a bright X-ray source has been found in *XMM-Newton* by Croston et al. (2004). This X-ray source, previously detected with *ROSAT*, was at first erroneously identified with a star which is offset by 20 arcsec from the X-ray source (Mason et al. 2000). A faint optical object coincident with the X-ray source has been detected in the Sloan Digital Sky Survey (the u-band magnitude is  $\approx 22$ ). Fig. A.1 shows the 327 MHz image of the faint radio source with resolution of  $7'' \times 6''$ . This image points out an extended low brightness emission between the two lobes in the region around the west side of the core. This implies the presence of low energy electrons in this region, which possibly might contribute to the IC emission. This emission was weakly detected in the image at 1.4 GHz. The total flux of the radio source at 327 MHz is  $\approx 93 \pm 2.5$  mJy. The angular extension is about one arcmin. Since there is no redshift measured for the optical counterpart, we could not provide an estimate of the linear dimensions or the equipartition magnetic field. The detection and the study of the low brightness emission of these kinds of sources, which show most of their emission in the low frequency range, is one of the main goals of the new generation of radio telescopes like LOFAR, SKA, LWA etc.

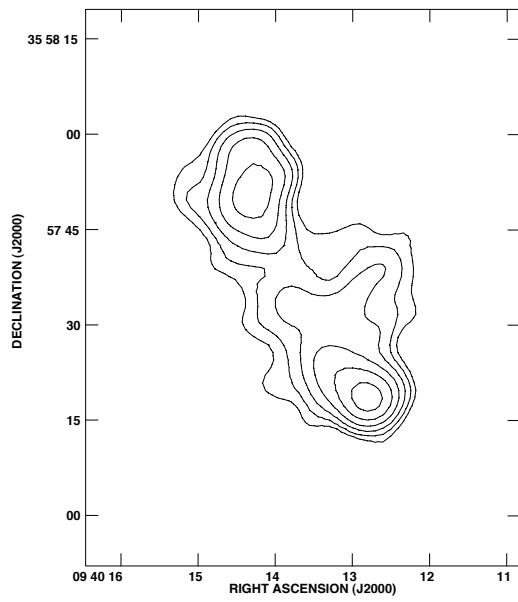


**Fig. A.1.** 327 MHz VLA image. The resolution is  $7'' \times 6''$  with a PA= $-78^\circ$ , contours start at  $(3\sigma)$  and are scaled by  $\sqrt{2}$ , the first level of contours is 1.8 mJy/beam.